A thermal bistability-based method for optimization of ultra-low threshold microlasers

Guoping Lin, Yves Candela, Olivier Tillement, Zhiping Cai, Valérie Lefèvre-Seguin, Jean Hare

A thermal bistability-based method for optimization of ultra-low threshold microlasers

Guoping Lin[1,2], Y. Candela[1], O. Tillement[3], Zhiping Cai[2], V. Lefvre-Seguin[1] and J. Hare[1]

[1] *Laboratoire Kastler Brossel, ENS, UPMC, CNRS – 24 rue Lhomond, 75231 PARIS cedex 05, France*
[2] *Department of Physics, Xiamen University, Xiamen 361005, Fujian, P. R. China*
[3] *LPCML, Universit Claude Bernard Lyon 1, 10 rue Andr-Marie Ampre, 69622 Villeurbanne cedex, France*
[*] *Corresponding author:* Jean.Hare@lkb.ens.fr

Compiled September 16, 2010

A method based on thermal bistability for ultra-low threshold microlaser optimization is demonstrated. When sweeping the pump laser frequency across a pump resonance, the dynamic thermal bistability slows down the power variation. This enables a realtime monitoring of the laser characteristic, for a functionalized microsphere exhibiting a sub-microwatt laser threshold. This approach is confirmed by comparing the results with a step-by-step recording in quasi-static thermal conditions.

OCIS codes: 140.3945, 140.3410, 140.3530, 140.6810, 130.3990

Optical microcavities have drawn a large interest in the last two decades and received numerous applications, including Cavity-QED (CQED) and photonic devices, like light emitting diodes or microlasers. A special attention has been devoted to molten silica microcavities induced by surface tension, like microsphere and microtoroids, which benefit from a sub-nanometer roughness, significantly smaller than for lithographically defined cavities. Their whispering gallery modes (WGMs) feature the highest quality factors (up to 10^{10} in the infrared), with moderate modal volumes down to about $100\lambda^3$. In a recent experiment J. Kimble and co-workers have demonstrated strong coupling regime of CQED for a microtoroid coupled to cold atoms [1].

For more practical applications, the weak coupling regime is also interesting, and the moderate coupling of a single emitter can be compensated by the collective coupling of several emitters. Hence the key property of silica microcavities is their very high quality factor, enabling laser operation with a pump power threshold in the microwatt range, or even less [2]. These ultra-low-threshold lasers have been obtained by silica functionalization with embedded rare earth ions (RE). Different RE doping techniques, like fiber doping, sol-gel coating, ion implantation, co-deposition or co-sputtering have been successfully used with Nd^{3+}, Er^{3+}, and Yb^{3+} or with mixtures [2–5].

In this paper, we focus on the new method we have developed to measure the optical pump–emission characteristic of a microlaser, taking advantage of the thermal effect induced by the pump laser. As is well known, a high quality factor monolithic cavity exhibits a thermal nonlinearity, due to self-heating by the minute optical power dissipated by internal losses. This nonlinearity leads to a thermo-optic bistability, with a very low threshold resulting from the high quality factor and the small heat capacity of the resonator [6–8]. We show that this provides a fast, efficient and accurate method to visualise, measure and optimize the laser characteristic. In this method, the pump laser frequency is not fixed on a resonance, but it is swept across a WGM resonance. The simultaneous monitoring of the injected power and the emitted signal directly provides the pump–microlaser characteristic, of which the threshold and differential efficiency are easily read out in realtime. For the first time, this approach is used to optimize the threshold and efficiency of microlasers. It is demonstrated on silica microspheres embedding neodymium-doped gadolinium oxide nanoparticules, which reproducibly feature sub-microwatt laser threshold.

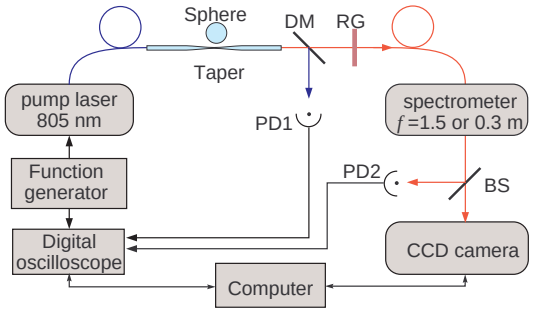

Fig. 1. (Color online) Sketch of the experimental setup. A free running laser diode is used as pump source to excite the RE in the microsphere. The pump laser and microlaser emission are denoted as blue and red, respectively. DM: dichroic mirror; BS: beamspliter; RG: Schott long pass filter RG850.

A sketch of the experimental setup is shown in Fig. 1. The heart of the experiment, where the microsphere is evanescently coupled to the fiber taper has been described in Ref. [9], as well as the microsphere fabrication by CO_2 laser melting of a thinned fiber. The fiber taper coupler is produced by pulling a single-mode optical fiber heated by a microtorch, as described in Ref. [10].

The functionalization is performed by using Nd doped Gd_2O_3 nanocrystals that are prepared by mixing Gd and Nd chloride and Sodium hydroxide in diethylene glycol. They are then transferred to alcohol to form a colloidal suspension [11]. The microsphere is dip-coated in this suspension and heated for a few seconds in order to anneal the nanoemitters and to embed them close to its surface, ensuring maximal coupling with low radial order WGM. The functionalized microspheres usually have Q-factors, measured by using a single-mode laser diode, ranging from 10^7 to 10^8 at pump wavelength $\lambda \approx 805$ nm and above 10^8 at emission wavelength $\lambda \approx 1083$ nm. Since aging problems due to water deposition is often observed, the 66 μm diameter silica microsphere described here was stored for a few days in order to achieve stable lasing conditions. Its quality factor was then reduced to 8.510^6 at pump wavelength and 4.710^7 at emission wavelength. These still very high figures lead to low threshold lasing and low threshold thermal bistability.

A free running laser diode (Sanyo DL-8141, $\lambda \simeq$ 805 nm) is coupled to the fiber taper and used to pump neodymium ions in the microsphere. As in Ref. [12], special care is taken to filter out a small fluorescence from this laser-diode in the 900-950 nm band thanks to a dispersion prism inserted between the pump laser and the input fiber coupler. The pump laser current and temperature are then adjusted to selectively excite a narrow linewidth WGM, that can be chosen of low angular order by using the method of Ref. [9]. On output, the transmitted pump is filtered out by the dichroic mirror and measured by the silicon detector PD1. After removal of the residual pump power by a longpass Schott filter RG850, the emitted light coupled out by the taper is analyzed in different ways. At first, we use a short focal length spectrometer (Acton SP300i, $f = 300$ mm) equipped with a spectroscopic camera (CCD1). With a 300 gr/mm grating, it records wide range spectra with a resolution of ~ 0.2 nm. The emitted signal can also be led by a fiber to a long focal length monochromator (Jobin Yvon THR1500, $f = 1.5$ m, 1200 gr/mm), the resolution of which, close to 0.01 nm, allows to resolve the fine structure of the peaks shown in Fig. 3 and to select a single mode of the laser signal. A beam splitter allows to send the transmitted beam to the InGaAs photodiode PD2 and to an high sensitivity EMCCD silicon camera CCD2 (Photometrics Cascade 512B).

To observe the onset of laser action, the absorbed power was first swept by using a stepwise method. This sweep is achieved by stepping the frequency of the pump laser diode. Due to thermal effect, this frequency change results in a slow variation of the power injected in the cavity, as shown in Fig. 2. The timing diagram of this step-by-step sweep is plotted in inset. As the time intervals ($\sim 0.1 - 0.6$ s), are much longer than the thermal time-constants ($\lesssim 15$ ms), each step corresponds to a steady-state operation. Emission spectra obtained on CCD1 for increasing absorbed power are plotted in 3-D in Fig. 3, and clearly evidence a multimode laser operation with a threshold of about 500 nW. This is confirmed by the inset of Fig. 3, where the area of the lasing peaks A and B, and of the 1054 nm photoluminescence (PL), are plotted as a function of the absorbed pump power. The PL clearly exhibits a quasi-saturation at threshold, an expected signature of population clamping.

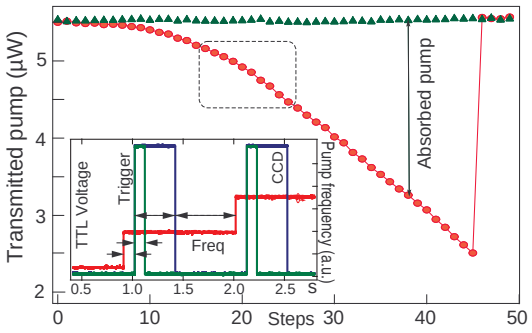

Fig. 2. (Color online) Transmitted pump (PD1) vs steps: the green triangles are the reference obtained for a large gap, and the red circles obtained for a gap of ~ 150 nm. The vertical arrow denotes the "absorbed pump power". Inset : time diagram, showing the TTL pulses used for synchronisation of the frequency steps (staircase shaped red curve), the exposure gate of the CCD and the measurement of PD1 signal. The delays represented by the horizontal arrows are in chronological order: settling time 0.1 s, PD1 measurement 0.1 s, CCD1 exposure time 0.4 s, CCD1 frame transfer delay 0.6 s.

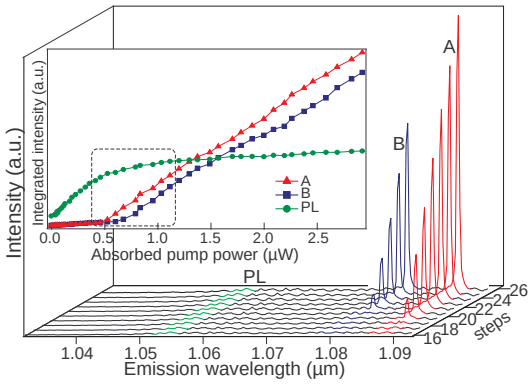

Fig. 3. (Color online) Emission spectra with increasing absorbed pump power for a limited step range (denoted by the doted rectangle in this figure and in the last one). Inset: Area of lasing peaks A and B (red triangles and blue squares respectively) and of PL (green circles). The PL signal is multiplied by a factor 10 for clarity.

To free ourselves from the multimode behavior, we use the high resolution spectrometer to filter out a single frequency. The lasing starting at ultra-low absorbed pump, we keep the incident pump power on the sphere lower than 10 μW in the whole experiment. We continuously scan the pump laser across a WGM resonance over a small frequency range of ~ 0.6 GHz. The transmitted

pump intensity measured on PD1 and the filtered laser signal measured on PD2 are simultaneously monitored on a digital oscilloscope, leading to the curves plotted in Fig. 4. In this figure, the pump signal (upper red curve) clearly exhibits a well-known thermal dynamical bistability, characterized by the asymmetry between the decreasing and increasing frequency periods. The black doted line is a best fit to the numerical solution of the differential equation for the temperature difference $\theta(t) = T(t) - T_0$:

$$\dot{\theta} = A\, P_{\rm inc}/(\Delta(t)^2 + (\gamma/2)^2) - \gamma_{th}\, \theta(t)\ , \qquad (1)$$

where the first term represents the heating, and the second the thermal leak. The heating is proportional (with a constant A) to the incident power $P_{\rm inc}$ and to a Lorentzian-shaped curve involving the effective detuning $\Delta(t) = \omega(t) - \omega_0 - K\theta(t)$, where $\omega(t)$ is the modulated frequency of the pump, and K the thermo-optic coefficient of the cavity. As in the precedent method, the baseline (green upper curve) has been first recorded with a large gap between the microsphere and the taper, and the absorbed pump power can be determined by subtracting the resonance dip from the baseline.

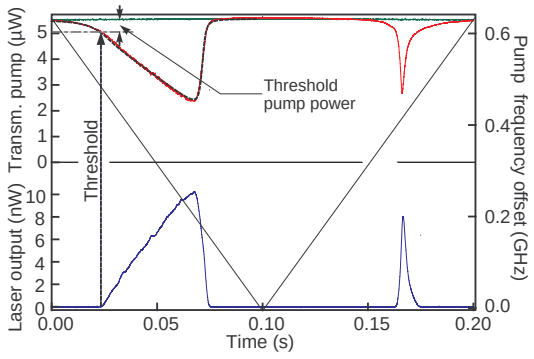

Fig. 4. Simultaneous recording of the absorbtion dip (upper red curve) and of the microsphere emission (lower blue curve). The triangle wave is the frequency modulation of the pump laser. The dotted line is a fit to the theoretical transmission curve deduced from Eq. (1).

As expected, the onset of microsphere emission (and underlined by the vertical arrow) occurs only when the absorbed pump signal reaches a finite value, which corresponds to the laser threshold. An X-Y plot, as used in Fig. 5, allows to measure the threshold and estimate the differential efficiency in *realtime*. Here the thermal effect provides a slow and smooth injected power variation, which has several advantages: *(i)* it allows the laser to adiabatically remain in steady state, *(ii)* it allows to work with a high sensitivity but low bandwidth InGaAs photodiode, *(iii)* the continuous sweeping weakens the noise due to the jitter of the pump laser.

To verify that the measured slope and threshold are actually those of the laser, we scan the pump laser at different repetition frequencies between 0.5 and 25 Hz. In

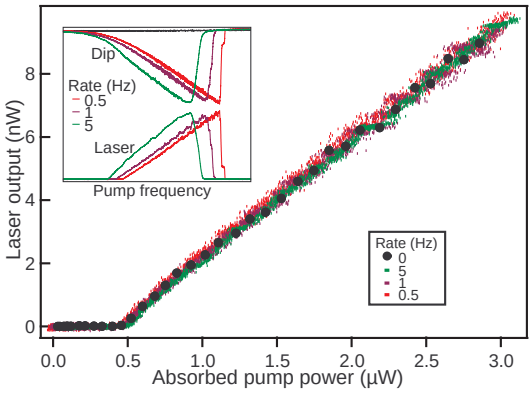

Fig. 5. Laser output power as a function of absorbed pump power, for different scan speeds (0.5, 1, 5 Hz) over the same range (0.6 GHz). Inset: corresponding transmitted pump and laser output curves.

Fig. 5, the obtained laser characteristics for 0.5, 1 and 5 Hz repetition rates are plotted on the same graph, demonstrating a very good consistence, despite their frequency-dependant shape, as shown in the inset. To confirm this result we make a last check, by using the step-by-step method and recording on PD2 the microlaser power transmitted by the high resolution spectrograph. The result is a steady state characteristic, plotted in Fig. 5 with open circles, and is in perfect agreement with the realtime characteristic. The scanning characteristics obtained at higher frequencies (above 10 Hz) are rather different because of the decreasing thermal effet and of the limited bandwidth of our detector.

In summary, we have developed two similar simple methods to characterize the laser characteristics microlasers based on rare earth emitters. Both methods take advantage of keeping a very high quality factor for the doped microcavities. This results in a strong thermal effect, allowing to control the pump power by the means of frequency sweeping. One of these methods can work at a rate as high as 10 Hz, allowing a realtime optimization of the coupling conditions. This promising approach allowed to demonstrate a sub-microwatt threshold neodymium-based laser, and will be applied for further optimizations to be published in a next future.

References

1. T. Aoki et al., Nature **443**, 671 (2006).
2. V. Sandoghdaret al., Phys. Rev. A **54**, R1777 (1996).
3. F. Lissillouret al., Electron. Lett. **36**, 1382 (2000).
4. L. Yang et al., Appl. Phys. Lett. **83**, 825 (2003).
5. E. Ostby et al., Opt. Lett. **32**, 2650 (2007).
6. V. B. Braginsky et al., Phys. Lett. A **137**, 393 (1989).
7. H. Rokhsari et al., Appl. Phys. Lett. **85**, 3029 (2004).
8. T. Carmon et al., Opt. Express **12**, 4742 (2004).
9. G. Lin et al., Opt. Lett. **35**, 583 (2010).
10. F. Orucevic et al., Opt. Express **15**, 13624 (2007).
11. R. Bazzi et al., J. Lumin. **113**, 161 (2005).
12. S. Steiner et al., Opt. Express **15**, 10053 (2007).

References

1. T. Aoki, B. Dayan, E. Wilcut, W. P. Bowen, A. S. Parkins, T. J. Kippenberg, K. J. Vahala, and H. J. Kimble, "Observation of strong coupling between one atom and a monolithic microresonator," Nature **443**, 671–674 (2006).
2. V. Sandoghdar, F. Treussart, J. Hare, V. Lefèvre-Seguin, J.-M. Raimond, and S. Haroche, "Very low threshold whispering-gallery mode microsphere laser," Phys. Rev. A **54**, R1777 (1996).
3. F. Lissillour, P. Feron, N. Dubreuil, P. Dupriez, M. Poulain, and G. M. Stephan, "Erbium-doped microspherical lasers at 1.56 μm," Electron. Lett. **36**, 1382–1384 (2000).
4. L. Yang, D. K. Armani, and K. J. Vahala, "Fiber-coupled erbium microlasers on a chip," Appl. Phys. Lett. **83**, 825–827 (2003).
5. E. Ostby, L. Yang, and K. Vahala, "Ultralow-threshold Ybˆ 3+: SiO_2 glass laser fabricated by the solgel process," Opt. Lett. **32**, 2650–2652 (2007).
6. V. B. Braginsky, M. L. Gorodetsky, and V. S. Ilchenko, "Quality-factor and non-linear properties of optical whispering-gallery modes," Phys. Lett. A **137**, 393–397 (1989).
7. H. Rokhsari, S. Spillane, and K. Vahala, "Loss characterization in microcavities using the thermal bistability effect," Appl. Phys. Lett. **85**, 3029 (2004).
8. T. Carmon, L. Yang, and K. Vahala, "Dynamical thermal behavior and thermal self-stability of microcavities," Opt. Express **12**, 4742–4750 (2004).
9. G. Lin, B. Qian, F. Oručević, Y. Candela, J. Jager, Z. Cai, V. Lefèvre-Seguin, and J. Hare, "Excitation mapping of whispering gallery modes in silica microcavities," Opt. Lett. **35**, 583–585 (2010).
10. F. Orucevic, V. Lefèvre-Seguin, and J. Hare, "Transmittance and near-field characterization of sub-wavelength tapered optical fibers," Opt. Express **15**, 13624–13629 (2007).
11. R. Bazzi, A. Brenier, P. Perriat, and O. Tillement, "Optical properties of neodymium oxides at the nanometer scale," J. Lumin. **113**, 161–167 (2005).
12. S. Steiner, J. Hare, V. Lefèvre-Seguin, and J.-M. Gérard, "Room temperature lasing of InAs/GaAs quantum dots in the whispering gallery modes of a silica microsphere," Opt. Express **15**, 10053–10060 (2007).